Ionic Dopant-Induced Ordering Enhances the Thermoelectric Properties of a Polythiophene-Based Block Copolymer

Ban Xuan Dong[1], Ziwei Liu[2], Jonathan W. Onorato[3], Tengzhou Ma[1], Joseph Strzalka[4], Peter Bennington[1], Christine K. Luscombe[3,5,6], Christopher K. Ober[2], Paul F. Nealey[1,7] and Shrayesh N. Patel[1,]*

[1]Pritzker School of Molecular Engineering, University of Chicago, Chicago, Illinois 60637, USA

[2]Department of Materials Science and Engineering, Cornell University, Ithaca, NY 14853, USA

[3]Department of Materials Science and Engineering, [5]Department of Chemistry, [6]Molecular Engineering and Sciences Institute, University of Washington, Seattle, WA 98195, USA

[4]X-ray Science Division, [7]Materials Science Division, Argonne National Laboratory, Lemont, Illinois 60439, USA

*Email: shrayesh@uchicago.edu

Keywords: Conjugated polymer-based block copolymers, ionic dopant, molecular dopant, organic thermoelectrics, Seebeck-conductivity relation.

ABSTRACT

Conjugated polymer based block copolymers (CP-BCPs) are an unexplored class of materials for organic thermoelectrics. Herein, we report on the electronic conductivity (σ) and Seebeck coefficient (α) of a newly synthesized CP-BCP, poly(3-hexylthiophene)-*block*-poly (oligo-oxyethylene methacrylate) (P3HT-*b*-POEM), upon solution co-processing with lithium bis(trifluoromethanesulfonyl)imide (LiTFSI), and subsequently vapor-doping with a molecular dopant, 2,3,5,6-tetrafluoro-7,7,8,8-tetracyanoquinodimethane (F4TCNQ). We found that the addition of the hydrophilic block POEM greatly enhances the processability of P3HT, enabling homogeneous solution-mixing with LiTFSI. Notably, interactions between P3HT-*b*-POEM with ionic species significantly improve molecular order and unexpectedly cause electrical oxidizing doping of P3HT block both in solution and solid states, a phenomenon that has not been previously observed in Li-salt containing P3HT. Vapor doping of P3HT-*b*-POEM-LiTFSI thin films with F4TCNQ further enhances σ and yields a thermoelectric power factor $PF = \alpha^2\sigma$ of 13.0 $\mu Wm^{-1}K^{-2}$, which is more than 20 times higher than salt-free P3HT-*b*-POEM sample. Through modelling thermoelectric behaviors of P3HT-*b*-POEM with Kang-Snyder transport model, the improvement in *PF* is attributed to higher electronic charge mobility originating from the enhanced molecular ordering of P3HT. Our results demonstrate that solution co-processing conjugated BCPs with a salt is a powerful method to control structure and performance of organic thermoelectric materials.

I. INTRODUCTION

Conjugated polymers (CPs) are an important category of electronic materials, and see a number of uses stemming from their solution processability, mechanical flexibility, stretchability, and the tunability of their physical properties *via* chemical modifications.[1–8] Doping CPs to modulate carrier concentration and control electronic conductivity is critical to enhancing performance of many optoelectronic devices. For instance, doping has been shown to facilitate trap-filling in organic field-effect transistors (OFETs), improve charge injection and collection in organic photovoltaics (OPVs) and organic light-emitting diodes (OLEDs).[9–13] Doping is of particular importance for organic thermoelectric applications, where the carrier concentration n impacts the electronic conductivity σ, the Seebeck coefficient α and the thermal conductivity κ, which all directly influence the thermoelectric figure of merit $ZT = \alpha^2\sigma T/\kappa$.[14–16] Optimizing thermoelectric performance in CPs thus requires fundamental understanding of the influence of chemistry, processing, and doping on both the polymer morphology and the resulting thermoelectric properties.

Electrical doping of CPs is usually achieved *via* electron transfer from the host polymer to molecular dopant in the case of p-type doping, or from the molecular dopant to the host polymer in the case of n-type doping. Typically, incorporating molecular dopants into the polymer affects not only the carrier concentration but also the polymer morphology, making it difficult to predict the change in electronic conductivity with dopant concentration.[17] Since the polymer-dopant interaction strongly depends on the way dopants are incorporated into the polymer samples, changing the doping method has a profound impact on σ , α and thermoelectric performance. For example, sequential doping methods where the polymer films is exposed to the dopant in vapor or solution phases[18–24] are shown to give superior electronic conductivity compared to solution doping where the polymer and dopant are co-processed from solution.[25,26] This improvement in electronic conductivity is due to the preservation of the underlying structure of the CPs after sequential doping. Compared to solution doped films, sequential doping of films of semiconducting polymers, such as poly(3-hexylthiophene) (P3HT) or copolymers of thiophene and thienothiophene (pBTTT), possess one to several orders of magnitude higher electronic conductivity.[22,27–30]

While significant efforts have been devoted to controlling and optimizing thermoelectric properties of CPs,[28,31–33] further improvement of the power factor, $PF = \alpha^2\sigma$, and reduction of the thermal conductivity, κ, are still needed to fully realize the potential of CP-based thermoelectrics. The most common strategy to overcome such limitations is to fabricate blends of CPs with other components such as different CPs, non-conjugated polymers, nanoparticles, or inorganic fillers.[34–36] Adding a secondary component to CP blends has been shown to improve charge transport,[37,38] enhance mechanical properties[37] and reduce thermal conductivity.[39] This improvement is usually driven by enhanced doping efficiency, better percolation of electronic conduction pathways and beneficial mechanical and thermal conductivity of the added components. Nevertheless, using conjugated polymer blends poses inherent challenges as they usually do not have well-defined and stable morphologies due to the phase separation between the different components, which can result in significant long-range heterogeneity in morphologies. Thus, an alternative replacement for CP blends is CP-based block copolymers, where the two components are covalently linked. While BCPs hold great potential for use in thermoelectrics, thus far there has been no detailed report on the structure-function relationships in molecularly doped BCPs for thermoelectric applications.

To this end, in this work we investigate the thermoelectric properties (σ and α) of poly(3-hexylthiophene)-*block*-poly (oligo-oxyethylene methacrylate) (P3HT-*b*-POEM) upon solution co-processing with lithium bis(trifluoromethanesulfonyl)imide (LiTFSI) and then vapor doping with the molecular dopant 2,3,5,6-tetrafluoro-7,7,8,8-tetracyanoquinodimethane (F4TCNQ). We find that while the thermoelectric *PF* of salt-free P3HT-*b*-POEM doped with F4TCNQ is lower than the homopolymer P3HT, co-processing P3HT-*b*-POEM with LiTFSI greatly improves its molecular order and thus electrical conductivity upon exposing to F4TCNQ vapor. As a result, *PF* as high as 13.0 $\mu Wm^{-1}K^{-2}$ is realized in P3HT-*b*-POEM at the intermediate LiTFSI blending concentration of r = [Li$^+$]/[EO] = 0.02. We rationalize the improvement in molecular order of P3HT-*b*-POEM to be due to the interaction between the oligoethylene glycol chains in the POEM segment with LiTFSI in solution prior to deposition, which lead to the formation of aggregates in solution and results in a higher degree of order in the resultant thin films.

II. RESULTS AND DISCUSSION

1. Structural control of P3HT-*b*-POEM *via* the addition of LiTFSI

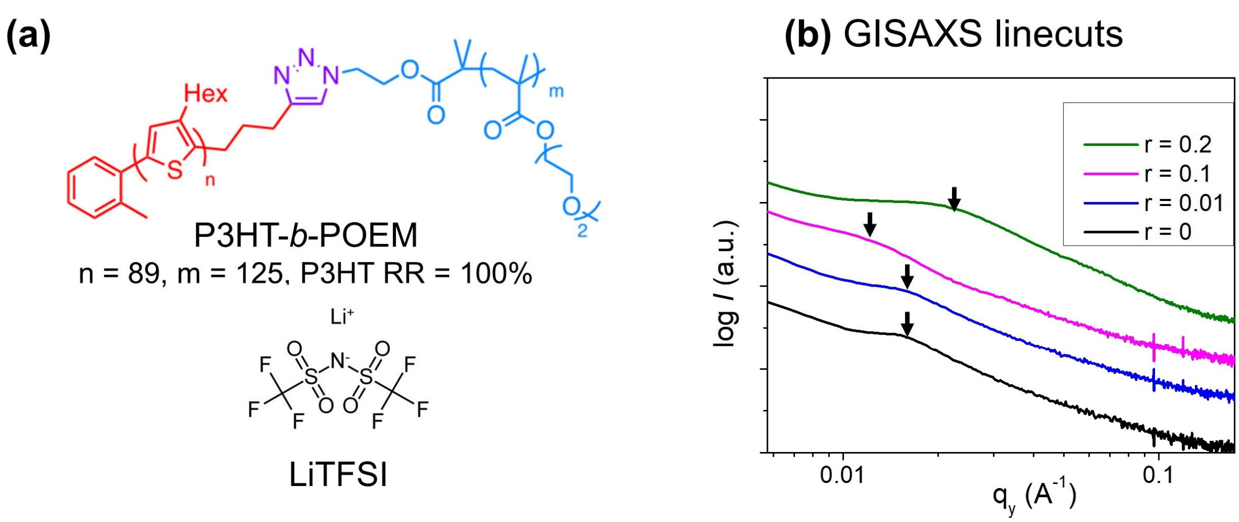

Figure 1: (a) Chemical structures of P3HT-*b*-POEM and LiTFSI. RR = regioregularity. (b) The GISAXS in-plane linecuts of P3HT-*b*-POEM-LiTFSI thin film samples (r = [Li$^+$]/[EO]). The arrow denotes the location of the primary scattering peak (q^*).

P3HT-b-POEM was synthesized by first synthesizing each block component separately. The P3HT block with trimethylsilane(TMS)-protected pentynyl end-groups via Kumada Catalyst Transfer Polymerization (KCTP) with an external initiator.[40] The POEM block was synthesized via Atom Transfer Radical Polymerization (ATRP). P3HT-b-POEM was then synthesized via CuAAC "click" reaction between P3HT and POEM blocks. More details of the synthetic procedures are shown in Supporting Information (Schemes 1 – 4 and Figures S1 – S2). In the first phase of our structural characterization investigation, we use a combination of grazing incidence small-angle and wide-angle X-ray scattering (GISAXS and GIWAXS) to study the self-assembly of P3HT-*b*-POEM upon the addition of LiTFSI. The chemical structures of both P3HT-*b*-POEM and LiTFSI are shown in Figure 1a. Here, we would like to note that coupling P3HT with the POEM block not only introduces additional functionalities but also helps to improve the solution processability of the materials due to the high solubility of POEM in various types of solvents. As an example, we show in the Supporting Information photographs (Figure S3) of P3HT-*b*-POEM-LiTFSI and P3HT-LiTFSI solution at the same LiTFSI solution volume ratio of *ca.* 30 %. Upon addition of LiTFSI solution, P3HT-*b*-POEM solution shows no visible macroscopic solution aggregation, in stark contrast to P3HT-LiTFSI solution where macroscopic particulates from polymer precipitation are clearly observed. AFM height images of P3HT-*b*-POEM-LiTFSI thin film (Figure S4) also show smooth (roughness < 2 nm) surface topography of all samples studied.

Figure 1b depicts the in-plane GISAXS profiles of P3HT-*b*-POEM-LiTFSI thin films at different LiTFSI concentration $r = [Li^+]/[EO]$ where EO is the number of repeated ethylene oxide units in the POEM block. The GISAXS profile of the salt-free ($r = 0$) sample only shows a weak, broad peak at $q^* = 0.015$ Å^{-1} which corresponds to a characteristic domain size ($d^* = 2\pi/q^*$) of 42 nm. This scattering profile is consistent with fibril-like domain P3HT structures that have been previously reported to form in P3HT-containing BCPs.[41–43] Upon adding LiTFSI, in-plane GISAXS exhibits similar scattering profiles, but d^* increases to 43 nm for $r = 0.01$ and 49 nm for $r = 0.1$. This increase in d^* likely arises from the preferential swelling of the POEM domain with LiTFSI. On the other hand, at $r = 0.2$, the GISAXS profile exhibits a broader q^* peak and the corresponding d^* is smaller at 31 nm. While the origin is unclear, we postulate that high salt loading likely leads to further disordering of the morphology and reduced d^*. Overall, the GISAXS profiles of P3HT-*b*-POEM with and without LiTFSI are indicative of weak phase separation and do not form traditional periodic nanoscale BCP morphologies. The strong crystallization of the P3HT block is the driving force behind the weak phase separation, a phenomenon which has been well-documented in CPs-containing BCP literature.[41–43]

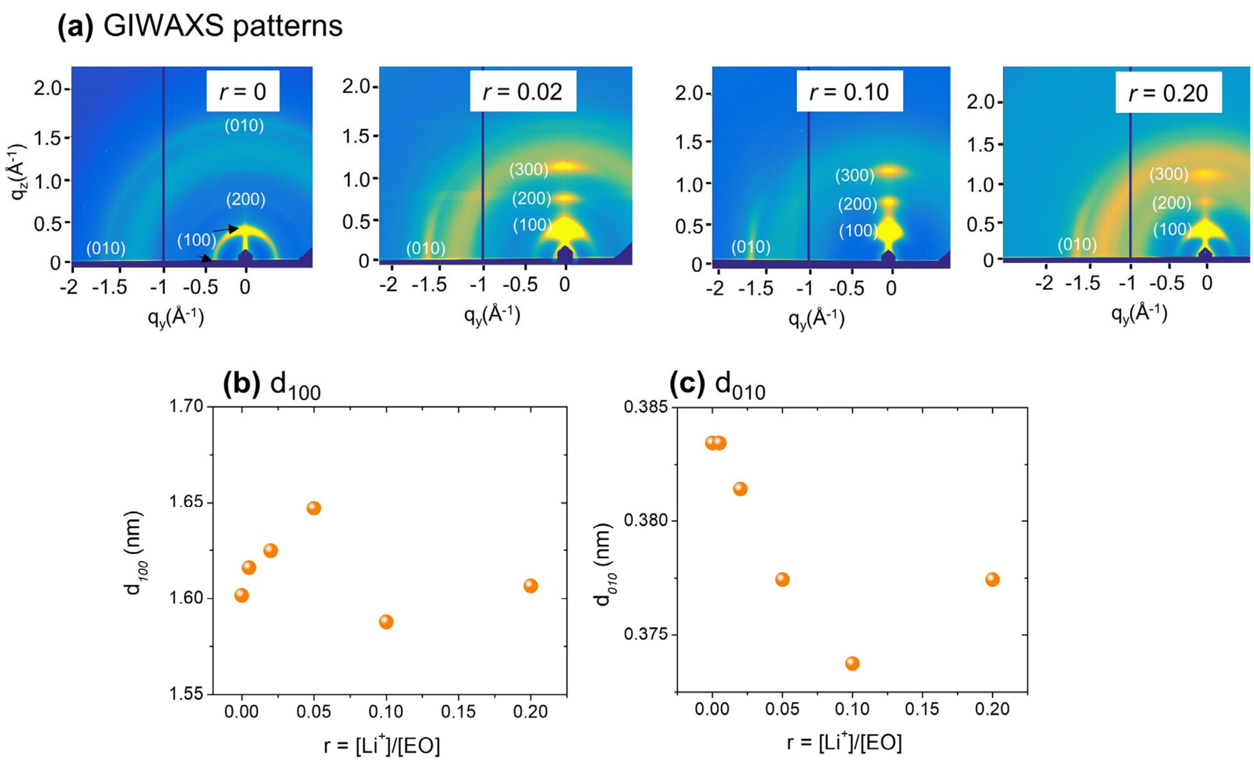

Figure 2: (a) Representative 2D GIWAXS images of P3HT-*b*-POEM thin films at different values of r. The complete set of GIWAXS images is shown in the Supporting Information. (b) and (c) Evolution of side-chain stacking distance d_{100} and π-stacking distance d_{010} as a function of r.

GIWAXS measurements were performed to probe the influence of LiTFSI on the molecular packing and ordering of the semicrystalline P3HT domain. Figure 2a shows the 2D GIWAXS images of P3HT-*b*-POEM-LiTFSI thin films at several representative values of r. GIWAXS images for all samples are shown in Figure S5. The GIWAXS pattern of the $r = 0$ sample contains scattering patterns from both the side-chain stacking direction (h00) and π-stacking direction (010). The sample intensity appears more ring-like between the in-plane and out-of-plane directions, indicating a nearly random orientation of crystallites. Note that POEM is amorphous and likely contributes to the diffuse scattering around $q \approx 1.3$ Å^{-1}. The addition of LiTFSI influences the molecular ordering and orientation of P3HT domain. In the $r = 0.02$ and 0.10 samples, the intensity of the (h00) and (010) peaks increase, indicating an increase in the relative degree of crystallinity (rDoC). In addition, we observe the (h00) reflections are predominately in the out-of-plane direction and the (010) reflection is predominately in the in-plane direction, which is indicative of stronger bias toward edge-on orientation of crystallites. At very high salt concentration of $r = 0.20$, the structure is still more locally ordered than the neat sample, but additional background scattering appears, which could originate from disordering of the polymer and/or excess amount of LiTFSI not dissolving into the polymer matrix. The changes in rDoC and crystallite orientation at different values of r can be further quantified by constructing a partial pole figure of the (100) reflection for each sample, as shown in Figure S6. The overall improvement of molecular order by the addition of a salt has been reported in the literature[44] and also shown in our previous works of oligoethylene glycol side chain-bearing polythiophene derivatives[45] and an oligothiophene-based liquid crystal with attached oligoethylene glycol chains.[24]

To provide more insights into structural evolution of P3HT-*b*-POEM upon adding LiTFSI, we show in Figure 2b and c the side-chain stacking distance d_{100} and π-stacking distance d_{010} as a function of r. The values of d_{100} and d_{010} were calculated by fitting the (100) and (010) peaks to a Lorentz function from out-of-plane and in-plane GIWAXS linecuts, respectively. As seen in Figure 2b and c, both d_{100} and d_{010} show non-monotonic changes in values with increasing r. From $r = 0$ to 0.05, d_{100} increases to 1.65 nm from the initial value of 1.60 nm, which might indicate that at least a portion of LiTFSI has infiltrated into the crystallite domain of P3HT despite the lower polarity of P3HT block compared to POEM block. Interestingly, the value of d_{100} drops to the original value of 1.60 nm at higher concentrations $r = 0.1$ and 0.2, perhaps due to changes in mixing behavior of LiTFSI and P3HT-*b*-POEM. On the other hand, d_{010} is found to reduce with r from 0.383 nm to 0.373 nm from $r = 0$ to $r = 0.1$ before slightly increasing to 0.377 nm at $r = 0.2$. Later on, we will show that this observation is due in part to the electronic doping effect of LiTFSI, leading to polaron formation, which in turn reduces the π-stacking distance.[46] The increase of d_{010} in $r = 0.2$ sample could be due to the highly disordered structure at this concentration, as is supported by UV-vis-NIR measurements described in the next section. Overall, these GIWAXS results reveal that the addition of a salt results in significant improvements in local molecular ordering of P3HT-*b*-POEM, which will have direct influence on electronic conductivity and thermoelectric properties of the materials.

2. Origin of improved molecular order of P3HT-*b*-POEM by the addition of LiTFSI

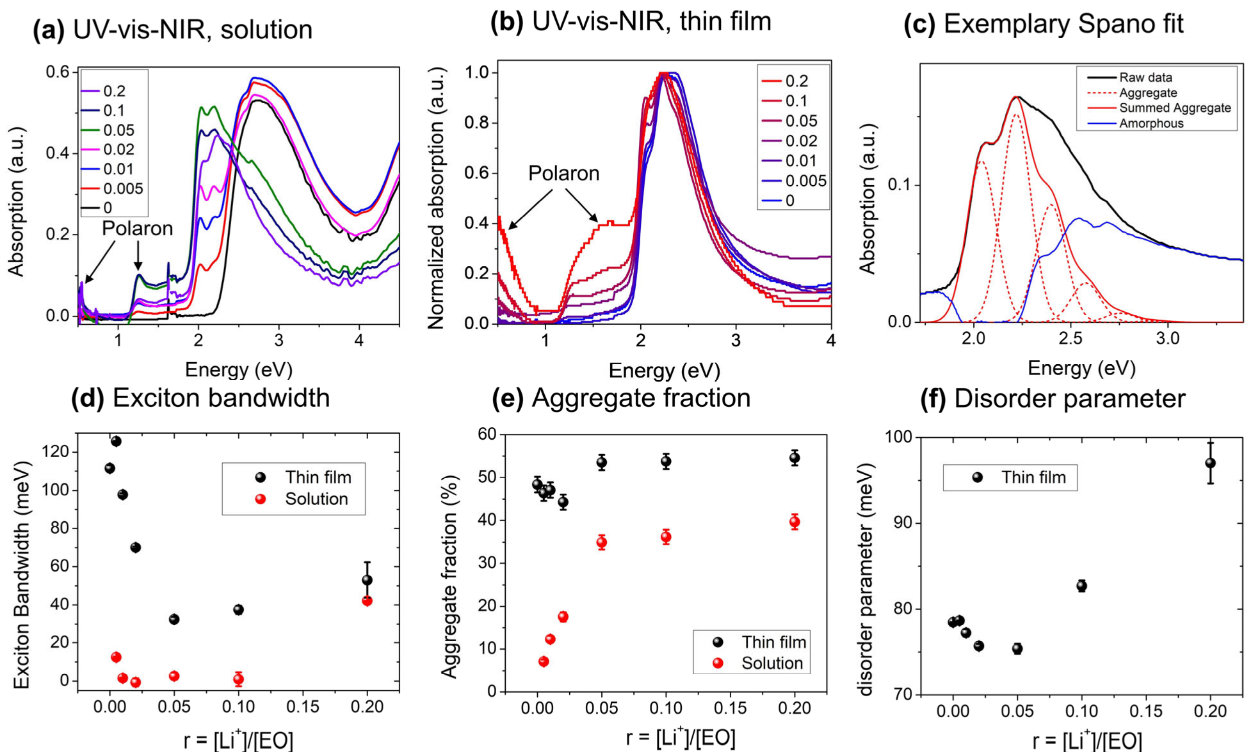

Figure 3: (a) Raw UV-vis-NIR absorption spectra of P3HT-*b*-POEM-LiTFSI in acetonitrile solutions and (b) Normalized UV-vis-NIR absorption spectra of P3HT-*b*-POEM-LiTFSI thin films. (c) Exemplary Spano fit performed on the $r = 0.02$ thin film sample. (d) Exciton bandwidth W, (e) fraction of aggregates and (f) disorder parameter σ_d extracted from Spano model fit.

To look into the origin of enhanced molecular order in P3HT-*b*-POEM by LiTFSI, we study the interaction of P3HT-*b*-POEM with LiTFSI both in the solution and thin film states using UV-vis-NIR absorption spectroscopy. Figure 3a and b show the absorption spectra of P3HT-*b*-POEM-LiTFSI in acetonitrile (AN) solutions and thin films, respectively. We use a quartz cell with very short path length of 100 μm, enabling absorption measurement of a solution that has the same concentration (10 mg/mL) as used to spin coat the thin film samples. The solution absorption spectrum of P3HT-*b*-POEM shows a single broad absorption peak near 3 eV which corresponds to the absorption of disordered P3HT. Upon solution blending with LiTFSI, we observe the appearance of aggregate peaks near 2 eV, the relative intensity of which initially increases with LiTFSI concentration from $r = 0$ to 0.05, but decreases at higher values of r. Similarly, the relative intensity of the aggregate peaks in P3HT-*b*-POEM thin films also increases until $r = 0.05$ and then decreases at higher r. Such an observation indicates the formation of π-stacked aggregates in solution upon adding LiTFSI. These aggregates in turn provide nucleation sites for crystal growth upon drying, and directly translates to higher crystalline order in solid state samples after spin-casting from solutions. Notably, in addition to the formation of aggregates in solution, the introduction of LiTFSI also leads to formation of polaron absorption peaks near 1.2 eV and 0.5 eV both in solution and solid state, indicative of electronic oxidizing doping of the P3HT block of P3HT-*b*-POEM (indicated by the black arrows in Figure 3a and b. The electronic doping is a surprising observation since LiTFSI is typically characterized as a redox-inactive ionic dopant. More details of this observation will be discussed further in the next section.

To quantify the observed solution and thin film ordering, we employ Spano model fit [47,48] on the UV-vis-NIR absorption spectra to deconvolute the contribution of amorphous and aggregate parts. A representative Spano model fit is shown in Figure 3c for the P3HT-*b*-POEM thin film at $r = 0.02$. From the fit, we extract three parameters of interest which are the exciton bandwidth W (Figure 3d), the aggregate fraction (Figure 3e) and the disorder parameter σ_d (Figure 3f). The aggregate fraction was calculated by comparing the absorption strength of the amorphous and aggregate portions using a previously reported procedure by Clark *et al*.[49] As can be seen in Figure 3d, adding LiTFSI significantly reduces W both in solution and thin film, with the minimum value of W achieved around $r = 0.02$ to 0.05. In the limit of weak excitonic coupling between co-facially packed polythiophene chains, the interchain coupling leads to the formation of vibronic bands characterized by W. A reduction of W is an indication of greater exciton delocalization across the polymer chains, and thus indicates a longer conjugation length. Notably, in solution we observe W approaches 0 within the limit of fitting error, indicative of fully extended, distortion-free P3HT chains in solution upon interaction with LiTFSI/AN solution. This highlights the positive impact of co-processing with LiTFSI/AN solution on improving molecular order of P3HT-*b*-POEM. The increase of W at very high value of r likely originates from the disorder induced by the excess amount of LiTFSI.

Interestingly, at the same r the value of W is always lower in solution compared to solid state, indicating that P3HT chains in solution on average have longer conjugation length compared to those in solid thin films. This difference is a surprising observation as the already-present aggregates in solution are expected to grow upon spin-casting from solution. This seemingly counterintuitive trend can be explained by comparing the fraction of aggregates in the solution and thin film samples, as shown in Figure 3e. At the same r, the aggregate fraction is always lower in solution, which suggests that there exist two populations of polymers: the highly extended polymer chains as already described, and also a substantial portion of polymer chains that are highly disordered. Upon spin-casting, those amorphous chains order to form fresh aggregates in the thin film in addition to the ones already formed in solution, leading to the lower average conjugation length observed in the thin film samples. Finally, as shown in Figure 3f, the disorder parameter σ_d for the thin film samples is also found to decrease to a minimum value near $r = 0.02 – 0.05$ before again increasing at higher r, similar to the trends observed for W.

Here, multiple factors are in play that control the extent of molecular ordering. We suspect that the formation of charged conjugated segments in solution provides attractive forces between adjacent chains which promotes aggregation, similar to the observation of improved ordering in mixed solutions of a conjugated polymer and molecular dopant.[20] An alternative explanation is the ionic crosslinking of the POEM block in the presence of LiTFSI which could bring the P3HT segments closer thus induce aggregation. It is important to note that in our experiments we used acetonitrile (AN) to dissolve LiTFSI prior to mixing with P3HT-*b*-POEM solution. Since AN is a poor solvent for P3HT, it is also possible that addition of AN is responsible for the aggregation.[50] To distinguish the effect of AN and LiTFSI, we perform a controlled experiment where we blend P3HT-*b*-POEM with only pure AN (without LiTFSI) at identical ratios as those used for the LiTFSI-containing mixtures. As detailed in Supporting Information section 5, at the same AN blending ratio, the addition of LiTFSI always induces more aggregate formation in solution compared to AN alone. We thus conclude that the improvement in P3HT-*b*-POEM molecular order originates from the combination of solubility factor of AN and doping effect of LiTFSI in solution prior to spin-casting.

3. The influence of LiTFSI on P3HT-*b*-POEM electronic conductivity

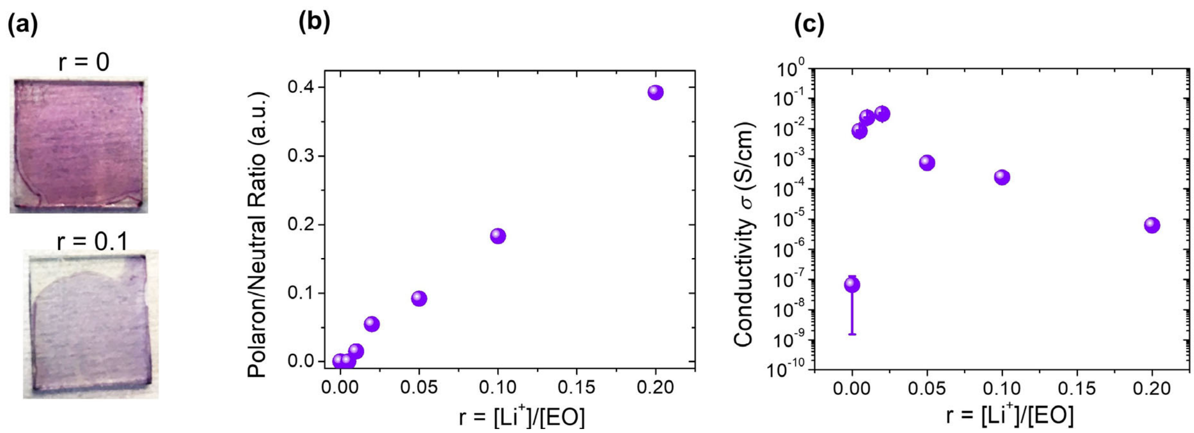

Figure 4: (a) Photographs of P3HT-*b*-POEM thin films without LiTFSI (top) and blended with LiTFSI at a concentration of $r = 0.1$ (bottom). The color bleaching of the thin film is indicative of LiTFSI doping P3HT. (b) Ratio between the polaron and neutral peak intensity extracted from UV-vis-NIR absorption spectra in Figure 3b and (c) electronic conductivity (σ) of P3HT-*b*-POEM thin film as a function of r.

Since we observe evidence of polaron formation in P3HT-*b*-POEM with LiTFSI, in this section we look further into the influence of LiTFSI on the σ of P3HT-*b*-POEM. We note that all the polymer thin film processing and conductivity measurements have been performed in an oxygen- and moisture-free argon-filled glovebox, thus we exclude the possibility of electronic doping due to exposure to ambient air. Shown in Figure 4a are photographs of P3HT-*b*-POEM thin films on a glass substrate, with (r = 0.1) and without LiTFSI (r = 0). As seen in Figure 4a, adding LiTFSI results in color bleaching of P3HT-*b*-POEM, providing another clear evidence of electronic oxidizing doping effect of LiTFSI. To further describe the relative degree of doping, we calculate the ratio of the polaron peak intensity near 0.5 eV and neutral peak intensity near 2.3 eV from the absorption spectra in Figure 3b (which we term as the polaron/neutral ratio), as done in prior studies.[22,51] The polaron/neutral ratio is found to linearly increase at function of r, suggesting an increase in doping level with addition of LiTFSI and the carrier/polaron concentration scales with LiTFSI concentration until r = 0.2. As shown in Figure 4c, σ of P3HT-*b*-POEM increases by more than 5 orders of magnitude from (6.5 ± 5) × 10^{-8} S/cm in the neat sample to (3 ± 0.2) × 10^{-2} S/cm in r = 0.02 samples before dropping to ca. 6.2 × 10^{-5} S/cm in r = 0.2 sample. We attribute the drop in σ at high r to disordering of P3HT induced by excessive amount of LiTFSI as indicated by UV-vis-NIR measurements (Figure 3).

Here, it is worth mentioning that the use of LiTFSI or other redox-inactive salts to improve electronic conductivity of organic semiconductors have been reported in literature.[24,44,52–55] The enhanced electronic conductivity in such cases have been attributed to factors such as changes in dielectric constant or improvements in molecular order caused by the addition of the ionic dopants. While there exist previous studies on LiTFSI doping of P3HT, [52,56,57] our results are distinctive as LiTFSI serves as an oxidizing dopant in P3HT-*b*-POEM leading to a higher doping level and, in turn, higher σ compared to these previous studies. The oxidizing doping behavior is demonstrated by for the presence of the polaron absorption peaks in the UV-vis-NIR (Figure 3b) and the decreasing d_{010} arising from the charged P3HT backbone (Figure 2c). Such structural changes were not observed in refs 52 and 56. Moreover, the resulting maximum σ in our P3HT-*b*-

POEM-LiTFSIis 3×10^{-2} S/cm at $r = 0.02$, which is substantially higher than the ones reported in ref 52 (~10^{-5} S/cm) and ref 56 ($10^{-7} - 10^{-6}$ S/cm). Overall, we believe our study is the first to report oxidizing doping behavior of a P3HT containing polymer with LiTFSI consistent with traditional dopants, which could have important implications in for the field of molecular doping. A complete understanding of the underlying mechanism for LiTFSI doping in P3HT-*b*-POEM will require probing local nano-scale distribution of ions, using different type of salts and different chemistry of non-conducting blocks, which is out of scope for this study.

4. Further improvement of electronic conductivity *via* vapor doping with F4TCNQ

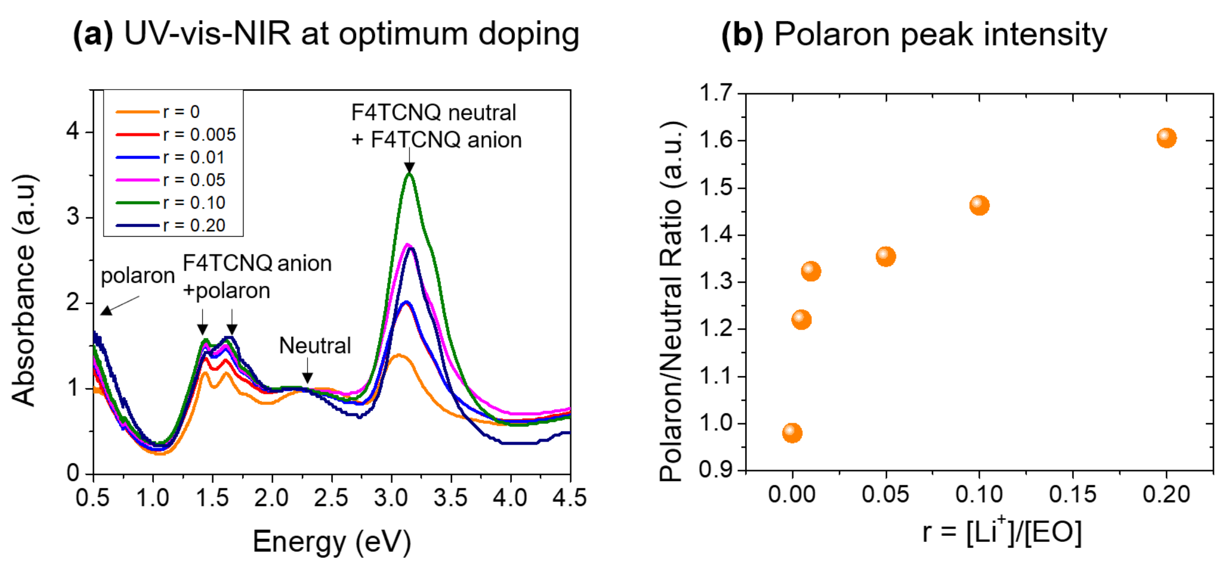

Figure 5: (a) Normalized UV-vis-NIR absorption spectra of different P3HT-*b*-POEM-LiTFSI samples at an optimal F4TCNQ doping condition of 5 min. (b) Ratio of polaron/neutral peak intensity extracted from (a).

While LiTFSI can electronically dope P3HT-*b*-POEM, the resulting σ is relatively low due to the low level of doping, as judged by the weak intensity of the polaron peak (Figure 4b). Therefore, to further increase σ to reach higher levels of thermoelectric performance, we further dope the thin films with the molecular dopant 2,3,5,6-tetrafluoro-7,7,8,8-tetracyanoquinodimethane (F4TCNQ). We note that different strategies of solution mixing and sequential doping have been employed to introduce molecular dopants such as F4TCNQ into conjugated organic semiconductors.[23,27,58] Here, we choose to follow the vapor doping method where one first casts a thin film of the polymer to be doped and then infiltrates F4TCNQ from the vapor phase. This method has been shown to lead to homogenous doping through the thickness of the thin film and minimal disruption of the underlying self-assembled structure of P3HT.[18,23,24,27]

UV-vis-NIR measurements revealed the extent of doping of P3HT-*b*-POEM-LiTFSI thin films after vapor doping with F4TCNQ (Figure 5a). An optimal doping time of 5 minutes was selected because the UV-vis-NIR absorption spectra remain unchanged above this time and σ levels out (as shown in later in Figure 7). As seen in Figure 5a, vapor doping the samples with F4TCNQ decreases the intensity of the neutral P3HT absorption peak near 2.3 eV, and leads to the appearance of new absorption peaks at 1.4 and 1.6 eV corresponding to the F4TCNQ anion and at 0.5 eV corresponding to the sub-band gap transition for polarons. The absorption structure from above 3.0 eV is a convolution of the F4TCNQ anion (~3.1 eV) and neutral F4TCNQ (~3.4 eV). These absorption features are consistent with the expected integer charge transfer (ICT) doping mechanism between P3HT and F4TCNQ.

To compare an approximate extent of doping between different P3HT-*b*-POEM-LiTFSI thin films, we took the peak intensity ratio between the polaron peak at 0.5 eV to the neutral peak. The addition of LiTFSI results in a positive impact on doping efficiency, evident by the increase in the polaron/neutral ratio with increasing LiTFSI concentration as shown in Figure 5b. The doping efficiency is highest in r = 0.2 sample despite its more disordered structure as indicated by UV-vis-NIR measurement. This observation suggests that degree of order is not the major factor affecting doping efficiency in the P3HT-*b*-POEM system investigated in this work. Note that the polaron/neutral ratio is also influenced by LiTFSI doping as demonstrated in Figure 4b. At the moment we are not able to separate the contribution from LiTFSI- and F4TCNQ-doping.

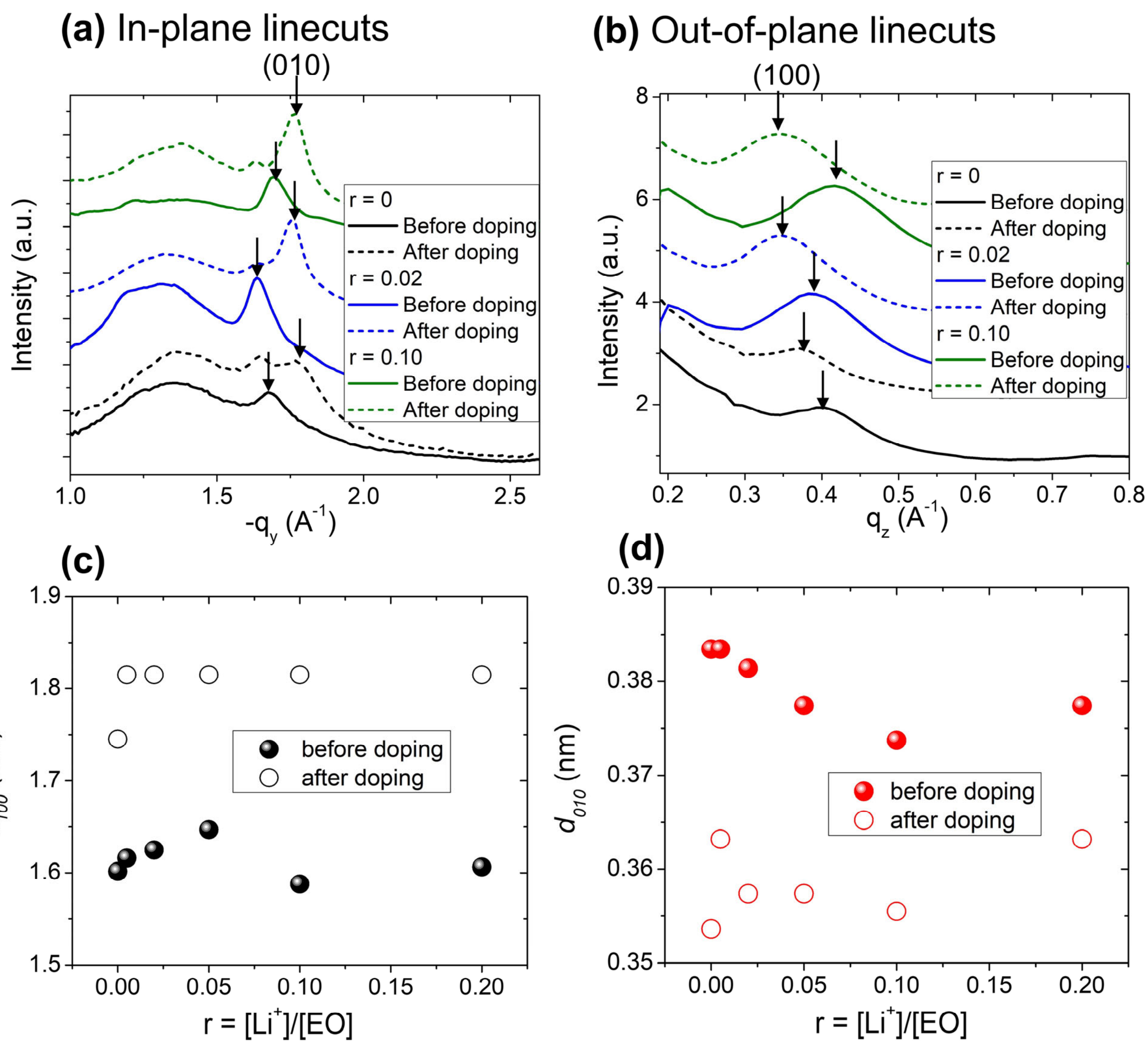

Figure 6: Representative (a) in-plane and (b) out-of-plane GIWAXS linecuts before and after 5 min of F4TCNQ doping. GIWAXS patterns of F4TCNQ-doped samples at all values of *r* are shown in the Supporting Information. (c), (d) Calculated values of d_{100} and d_{010} of different P3HT-*b*-POEM-LiTFSI samples before and after 5 min doping with F4TCNQ vapor.

GIWAXS measurements were performed to understand the influence of F4TCNQ vapor doping on the molecular packing of P3HT-*b*-POEM-LiTFSI thin films. For the P3HT-*b*-POEM-LiTFSI thin films, F4TCNQ vapor doping does not lead to significant disruption of the underlying molecular packing structure, as indicated by similar GIWAXS patterns before and after vapor doping with F4TCNQ (Figure S5 and S7). The notable changes correspond to the location of the (100) and (010) peaks as seen through the in-plane and out-of-plane linecuts acquired from the 2D GIWAXS images (Figure 6a and b) and quantified through calculation of d_{100} *and* d_{010} (Figure 6c and d). A table of *d*-spacing values of all the samples before and after doping with F4TCNQ is shown in the Supporting Information (Table S1). As observed in the in-plane linecuts, the π-stacking peak (010) shifts to higher *q* for all samples after doping with F4TCNQ (indicated by the arrows in Figure 6a). The shift of the (010) peak to higher *q* is indicative of the reduction in the π-stacking distance upon doping. This reduction is due to the delocalization of polarons between adjacent chains, leading to attractive forces that reduce the π-π spacing.[46] Importantly, for LiTFSI-blended samples at $r = 0.02$ and $r = 0.10$, the relative intensity of the π-stacking peak after doping is much higher than the neat sample, highlighting the interplay between LiTFSI and F4TCNQ, and the importance of the two dopants in increasing overall doping efficiency. The final d_{010} is *ca.* 0.35 – 0.36 nm for all samples which is similar to the value reported in literature for F4TCNQ-doped P3HT homopolymer.[22] On the other hand, the out-of-plane linecuts shown in Figure 6b indicate a shift in the (100) peak to lower *q* after F4TCNQ doping. The shift in *q* value corresponds to the increases in d_{101} from *ca.* 1.6 nm to *ca.* 1.8 nm after doping for all samples, values which are also similar to the reported value of fully-doped P3HT homopolymer.[22] The increase in the side-chain *d*-spacing is due to the intercalation of F4TCNQ into P3HT side-chains.[20,22,23] Our combined UV-vis-NIR in Figure 5, GIWAXS data in Figure 6, together with the depth-profile probed by GIWAXS (Figure S8) suggests that F4TCNQ penetrates the whole film thickness and efficiently dopes the P3HT block even in the presence of the POEM and LiTFSI.

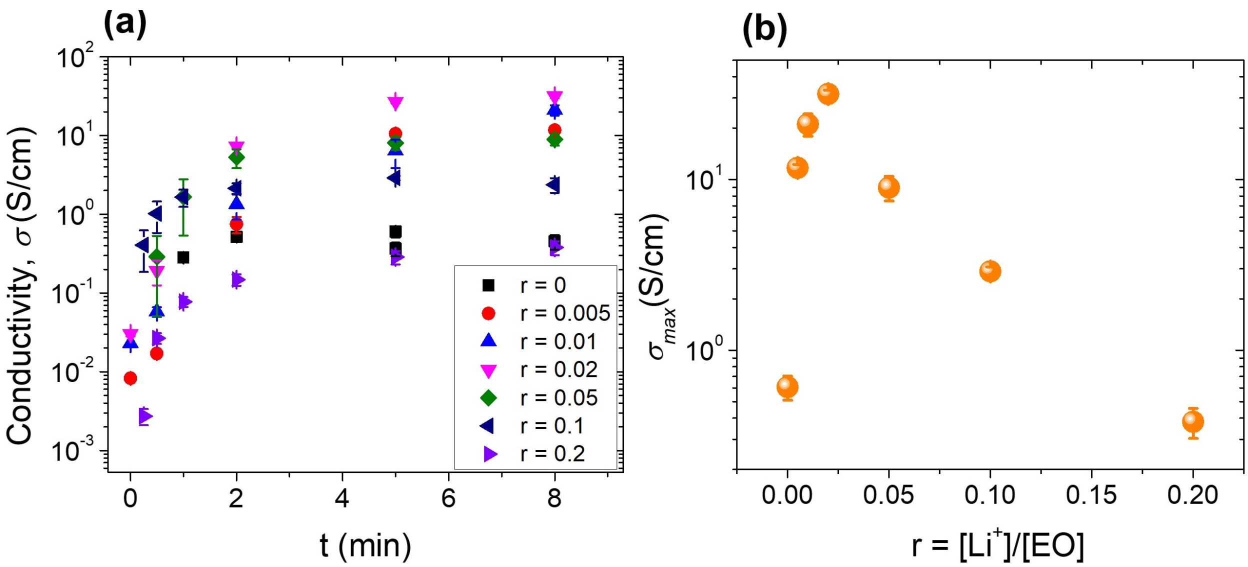

Figure 7: (a) Electronic conductivity (σ) of different P3HT-b-POEM-LiTFSI thin films as a function of F4TCNQ vapor doping time. (b). Maximum electronic conductivity (σ_{max}) of each F4TCNQ-doped P3HT-*b*-POEM-LiTFSI thin films.

Having demonstrated that F4TCNQ vapor doping is an effective method to introduce electronic carriers into P3HT-*b*-POEM-LiTFSI thin films while maintaining the molecular ordering, we proceed to measure σ as a function vapor doping time (Figure 7a). Upon exposing the samples to F4TCNQ vapor, σ quickly rises, levels out around 5 min of doping. To emphasize the effect of r on σ of the samples, we plot in Figure 7b the maximum electronic conductivity ($\sigma_{\max}$) obtained for each F4TCNQ-doped P3HT-*b*-POEM-LiTFSI thin film as a function of r. The value of σ for the salt-free (r = 0) sample is 0.61 ± 0.10 S/cm, which is more than an order of magnitude lower than the σ of 14.7 ± 1.7 S/cm of the exact same P3HT homopolymer block we used to synthesize the P3HT-*b*-POEM BCP. We attribute the lower σ of the neat sample to the highly disordered morphology of P3HT-*b*-POEM sample compared to P3HT homopolymer sample based on the results of the GIWAXS measurements and the presence of the electronically insulating POEM block that impedes charge transport (See Supporting Information Figure S9). Upon introducing LiTFSI, the maximum conductivity quickly rises, which the highest σ of 31.6 ± 1.8 S/cm achieved in r = 0.02 sample. When normalizing to the P3HT volume fraction, an effective σ

of *ca.* 83 S/cm is obtained, which surpasses the σ of P3HT homopolymer (Details of volume fraction calculation is shown in Supporting Information Figure S11). The improvement in σ in the low r regime could originate from a combination of multiple factors: (i) improved molecular order, (ii) the presence of carrier concentration induced by LiTFSI doping, and (iii) increasing doping efficiency with F4TCNQ. For $r > 0.02$, σ monotonically decreases with increasing r. Since the doping efficiency still increases with r (Figure 5b), the drop in σ at high value of r is likely caused by a reduction in the apparent charge carrier mobility arising from the higher degree of disorder determined through the UV-vis-NIR analysis, and/or the $TFSI^-$ and $F4TCNQ^-$ counter ion scattering effect that can negatively impact carrier mobility.[59–61] We note that, since $TFSI^-$ and $F4TCNQ^-$ counter ions are likely to at least partially reside in the POEM domains, the scattering effects in our case are expected to be weaker than in cases of homopolymer doping.

5. Improving thermoelectric properties through the addition of LiTFSI

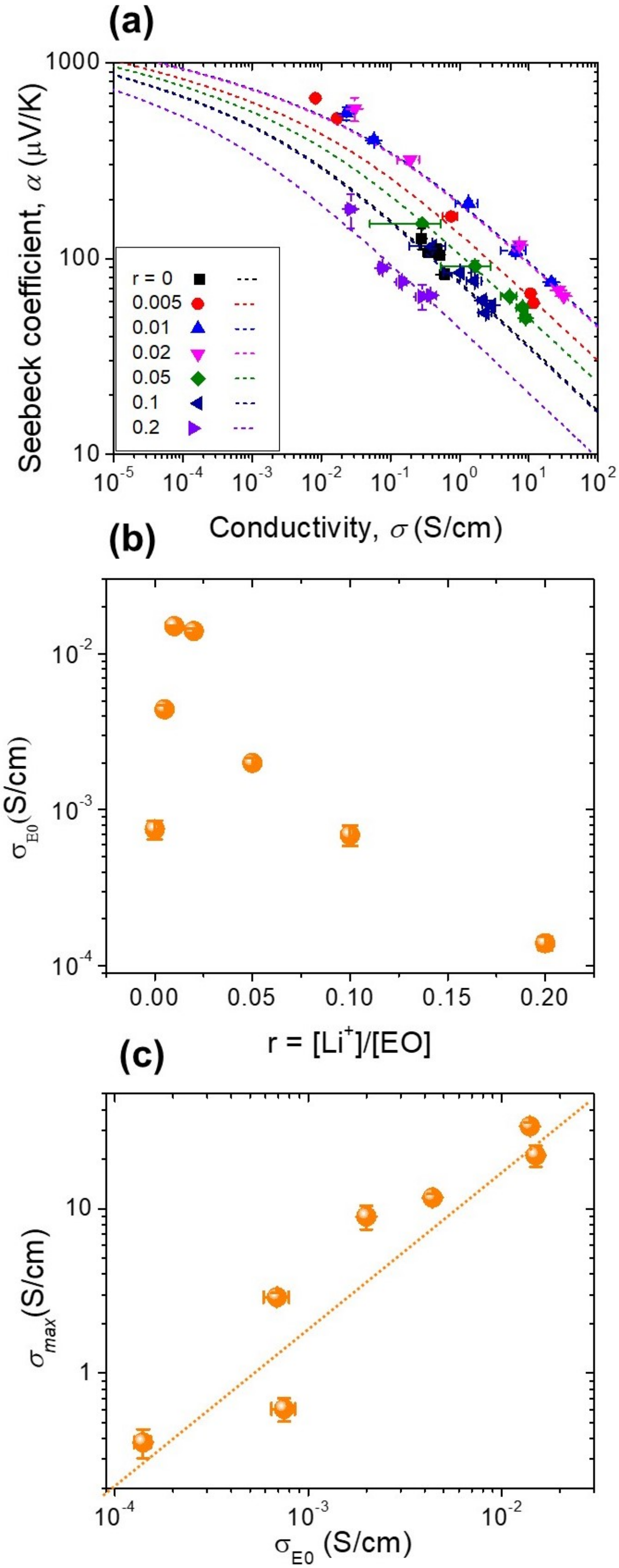
(a)
Seebeck coefficient, α (μV/K)
Conductivity, σ (S/cm)
r = 0
0.005
0.01
0.02
0.05
0.1
0.2
1000
100
10
10^-5
10^-4
10^-3
10^-2
10^-1
10^0
10^1
10^2
(b)
σ_E0 (S/cm)
r = [Li+]/[EO]
10^-2
10^-3
10^-4
0.00
0.05
0.10
0.15
0.20
(c)
σ_max (S/cm)
σ_E0 (S/cm)
10
1
10^-4
10^-3
10^-2

Figure 8. (a) Correlation between Seebeck coefficient and conductivity for different P3HT-*b*-POEM-LiTFSI thin films after vapor doping with F4TCNQ. The solid symbols represent experimental data. The dashed lines at each color represents the fit of Kang and Snyder's charge transport model to the experimental data set of the same color. The fits were performed using s = 3 (see more details in the text). (b) The fitted results of σ_{E0} from Kang and Snyder's model in (a) for each P3HT-*b*-POEM-LiTFSI thin film. The error bar for each value of σ_{E0} was calculated from the uncertainty of the fit. (c) Correlation between the maximum measured conductivity σ_{max} in Figure 7b and the fitted values of σ_{E0} at each value of r. The dashed line is guide to the eyes.

The benchmark figure of merit, ZT, for thermoelectric materials depends on α, σ, and κ, according to $ZT = \alpha^2\sigma T/ \kappa$. In this equation, the numerator $\alpha^2\sigma$ represents the power factor, PF, of a material at given α and σ values. While σ describes transport of a carrier under influence of an electric field, α describes the migration of charge carriers under a temperature gradient. The PF of a material is related to the Fermi level within the electronic density of state (DOS) and carrier scattering processes.[62] To understand the correlation between σ and α of the F4TCNQ-doped P3HT-*b*-POEM-LiTFSI thin films, we plotted α as a function of σ on the log-log scale (Figure 8a). Fundamentally, one can express σ and α of a system as a sum of contribution of states at each energy E using the following equations:[63]

$$\sigma = \sigma_E \left(-\frac{\delta f}{\delta E}\right) \mathrm{d}E \ (1)$$

$$\alpha = \frac{k_B}{e} \int \frac{E-E_F}{k_B T} \frac{\sigma_E}{\sigma} (-\frac{\delta f}{\delta E}) \mathrm{d}E \ (2)$$

Here, σ_E is the transport function, $f(E)$ is the Fermi-Dirac distribution, whereas E_F, k_B, e, T are the Fermi energy level, Boltzmann constant, elementary charge and temperature, respectively. Generally, both α and σ depend on the carrier concentration n *via* E_F but these dependencies have opposite trends: increasing n fills more states and increases σ but also brings E_F closer to those transport states and thus, decreasing α. Expectedly, for all samples, α is found to decrease with increasing σ as shown in Figure 8a. Similar slopes were observed for all $\alpha - \sigma$ data, suggesting similar transport mechanism among the samples. Additionally, from $r = 0$ to 0.02, we observe a gradual "right" shift of $\alpha - \sigma$ curves where σ values are observed to increase at the same corresponding α value; whereas for r equal or large than 0.05, the trend reverses as the $\alpha - \sigma$ curves shift to the left where σ values decrease for a given value of α.

To further understand the transport mechanism in the F4TCNQ-doped P3HT-*b*-POE/LiTFSI samples, we model the $\alpha - \sigma$ relation using a theoretical model proposed by Kang and Snyder.[64,65] While recently there exists more complex transport models built upon this original model that can further capture localized/delocalized transports or influence of disorder,[66,67] we choose to use the original Kang-Snyder model since this model is simple yet has been shown to successfully model thermoelectric properties of a wide range of CPs and can be used to extract our mobility-related parameter of interest σ_{E_0} as described further below. The Kang-Snyder model assumes that above a transport edge E_t, σ_E has a power law energy dependence with the power s but below E_t, carriers are completely localized and do not contribute to the transport as follows:

$$\sigma_E(E,T) = \sigma_{E_0}(T) \times \left(\frac{E - E_t}{k_B T}\right)^s \quad (E > E_t)$$

$$= 0 \; (E < E_t) \qquad (3)$$

Notably, as shown in equation 3, the Kang-Snyder model needed only two parameters σ_{E_0} and s to successfully model $\alpha - \sigma$ data for a wide range of organic semiconductors.[64] Here, σ_{E_0} is energy-independent and functions as a weighted mobility and thus determines the magnitude of σ. Importantly, σ_{E_0} can be directly related to the charge carrier mobility without knowledge of carrier concentration n. On the other hand, s determines the magnitude of energy-dependency of σ, where $s = 1$ is typical for 3-dimensional crystalline solids but $s = 3$ can be expected when charge carriers are scattered by ionized impurities such as molecular dopant anions and other salts.[64] To fit our $\alpha - \sigma$ data to the Kang-Snyder model, we systematically change s from 1 to 3 and then fit each of the $\alpha - \sigma$ dataset to find σ_{E_0}. In our case, fitting to Kang-Snyder model using s = 3 gives the better fit than s = 1 or 2 for all the $\alpha - \sigma$ data, indicating a strong energy dependence of charge transport above E_t, which is similar to many other organic semiconductors reported in literature.[64,65] The fits of the data to the Kang-Snyder model with s = 3 are shown as dashed lines in Figure 8a and the fits with s = 1 and s = 2 are shown in the Supporting Information (Figure S12 and 13).

Plotted in Figure 8b is the σ_{E_0} values from the Kang-Snyder fit for each F4TCNQ-doped P3HT-*b*-POEM-LiTFSI thin film using s = 3. As shown in Figure 8b, σ_{E_0} is increase from (7.5 ± 1.04) × 10^{-4} to (1.5 ± 0.13) × 10^{-2} S/cm from r = 0 to 0.02 then reduce to (1.4 ± 0.14) × 10^{-4} S/cm from r = 0.02 to r = 0.2. This trend agrees with the qualitative observation from the raw data in Figure 8a, in which the "right" shift and "left" shift of the $\alpha - \sigma$ curve are indicative of higher and lower values of σ_{E_0}, respectively.[64] As of note in the Kang-Snyder model, the trend in σ_{E_0} can be directly related to the trend in the charge carrier mobility. Meaning, higher values of σ_{E_0} correlates to higher charge carrier mobility. We show in Figure 8c the correlation between the measured maximum conductivity σ_{max} of F4TCNQ-doped P3HT-*b*-POEM-LiTFSI thin films (Figure 7b) and the fitted value of σ_{E_0} (Figure 8b). σ_{max} is shown to correlate well with σ_{E_0}, indicating that the improved σ_{max} likely originates from the high carrier mobility induced by enhanced molecular order upon addition of LiTFSI. Overall, we have shown that modeling of $\alpha - \sigma$ relationship can give valuable information about trends in carrier mobility of the samples which can be challenging to measure by other means.

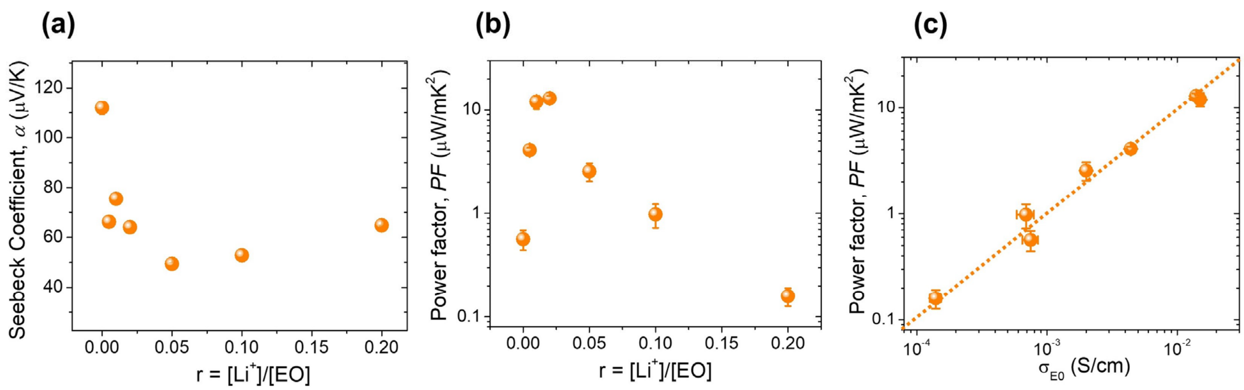

Figure 9. (a) The Seebeck coefficient (α) of vapor F4TCNQ-doped P3HT-*b*-POEM-LiTFSI samples at optimum doping condition (~ 5 min). (b) The Power Factor (*PF*) of 5 min-doped P3HT-*b*-POEM-LiTFSI samples. (c) Correlation between measured *PF* and fitted σ_{E_0} shown in Figure 8b. The dashed line is guide to the eyes.

Finally, we compute the power factor $PF = \alpha^2\sigma$ to study the influence of LiTFSI on the thermoelectric properties of F4TCNQ-doped P3HT-*b*-POEM-LiTFSI thin films. The *PF* of all samples across the whole conductivity range is shown in Supporting Information Figure S14. In Figure 8d we show the maximum *PF* of F4TCNQ-doped P3HT-*b*-POEM-LiTFSI system at different values of *r*. The *PF* quickly increases by more than an order of magnitude from 0.6 ± 0.1 μWm^{-1}K^{-2} at $r = 0$ to a maximum value of 13.0 ± 0.7 μWm^{-1}K^{-2} at $r = 0.02$ before decreasing at higher salt concentrations. This optimized PF values is ca. 50% higher than the optimized *PF* of F4TCNQ-doped P3HT homopolymer of 8.1 ± 1.0 μWm^{-1}K^{-2} (See Figure S15).

To see whether the enhancement in *PF* originate from changes in α, we plotted in Figure 9b the value of α for the optimal F4TCNQ doping time of 5 min. As seen in Figure 9b, α is found to reach a minimum near $r = 0.05$ before slightly increasing at higher LiTFSI concentration. The salt-free ($r = 0$) sample has the highest α of 112.0 ± 2.8 μV/K; the $r = 0.05$ sample has the lowest α of 49.5 ± 0.6 μV/K whereas the $r = 0.1$ and 0.2 samples have the values α of 52.8 ± 1.0 μV/K and 64.8 ± 0.2 μV/K, respectively. The trend of α from $r = 0$ to 0.05 can be explained by the increase in doping efficiency/carrier concentrations with *r* as demonstrated in Figure 5b. The slight increase of α at high salt concentration could originate from the broadening of the DOS, or could be due to the influence of ion movement; the exact cause is as-yet unclear. However, similar to a previous study,[22,27] it is evident that α is not as sensitive to the morphology of the materials as conductivity, only varying from *ca.* 50 μV/K to *ca.* 110 μV/K across the whole range of *r*. Overall, we attribute the improvement of *PF* is dominated by the increase in σ. Indeed, similar to σ, the measured *PF* shows strong correlation with σ_{E_0}, as demonstrated in Figure 9c.

III. CONCLUSION

In conclusion, we explored how solution co-processing the block copolymer P3HT-*b*-POEM with LiTFSI controls the molecular ordering and resulting thermoelectric properties. Overall, co-processing P3HT-*b*-POEM with LiTFSI solution led to an initial marked enhancement in molecular order, as shown by both GIWAXS and UV-vis-NIR absorption spectroscopy before dropping at high LiTFSI concentration. We attributed this improvement to the interaction between LiTFSI/AN and P3HT-*b*-POEM chains in solution, leading to the formation of P3HT aggregates in solution. This pre-aggregation results in highly ordered P3HT-*b*-POEM-LiTFSI thin films. In addition, blending P3HT-*b*-POEM with LiTFSI resulted in electronic doping of P3HT-*b*-POEM, leading to a more than 5 orders of magnitude increase in electronic conductivity. Due to the increase in molecular order, the F4TCNQ-vapor doped P3HT-*b*-POEM-LiTFSI thin film yielded σ as high as 31 S/cm at r = 0.02, which is *ca.* 50 times larger than the neat thin film (r = 0). By correlating experimental α and σ through a model proposed by Kang and Snyder, we showed that the enhanced σ resulted from improved charge carrier mobility of the LiTFSI-containing P3HT-*b*-POEM thin films. This translated to a *PF* of 13.0 $\mu Wm^{-1}K^{-2}$ compared to the value of 0.6 $\mu Wm^{-1}K^{-2}$ in the neat P3HT-*b*-POEM sample. Our results demonstrate that co-processing conjugated polymers with ionic dopants to control molecular ordering can be a powerful strategy in modulating thermoelectric material properties.

IV. ACKNOWLEDGEMENT

This work was supported by NSF DMREF Award Number 1629369. This research used resources of the Advanced Photon Source; an Office of Science User Facility operated for the U.S. Department of Energy (DOE) by Argonne National Laboratory under Contract No. DE-AC02-06CH11357. This work made use of the Cornell Center for Materials Research Shared Facilities which are supported through the NSF MRSEC program (DMR-1719875). Parts of this work were carried out at the Soft Matter Characterization Facility of the University of Chicago. This work made use of the Pritzker Nanofabrication Facility part of the Pritzker School of Molecular Engineering at the University of Chicago, which receives support from Soft and Hybrid Nanotechnology Experimental (SHyNE) Resource (NSF ECCS-2025633), a node of the National Science Foundation's National Nanotechnology Coordinated Infrastructure.

V. CODE AVAILABILITY

The MATLAB code used to fit Kang-Snyder model is available upon reasonable request to the corresponding author.

VI. EXPERIMENTAL

1. Materials and sample preparation

Detailed synthesis of P3HT-*b*-POEM are shown in Supporting Information (Schemes 1 – 4 Figure S1 – S2). LiTFSI (battery grade) was purchased from Sigma Aldrich and dried in high vacuum for 24 h before using. Anhydrous chloroform and acetonitrile were also purchased from Sigma Aldrich and used as received.

Solutions of P3HT-*b*-POEM and LiTFSI were prepared by dissolving the materials in anhydrous chloroform and anhydrous acetonitrile, respectively, at a concentration of 10 mg/mL and stirred overnight. P3HT-*b*-POEM solution was then filtered through a 0.45 μm filter before mixing with LiTFSI solution to achieve P3HT-*b*-POEM-LiTFSI mixed solution at different LiTFSI concentration. The mixed solutions were then spin-casted under argon atmosphere onto the prepared substrates at 2000 rpm for 2 min. Film thicknesses of all samples in this study were kept at *ca.* 60-70 nm, as confirmed by spectroscopic ellipsometry measurements. Prior to sample deposition, all substrates were cleaned by sonication in acetone and isopropanol for 15 min each and then exposed to oxygen-plasma cleaning for 10 min.

2. F_4TCNQ vapor doping procedure

Vapor-doping of F_4TCNQ was performed in an argon-filled glove box. Approximately 5 mg of dopant were placed in a small ceramic crucible within a glass jar (diameter, ~5 cm; height, ~4.5cm) and then the glass jar was inserted into a preheated stainless-steel container for at least 30 min on top of a hotplate. The temperature of the hotplate was set to 220 °C which was shown to be the optimum temperature for sublimation of F_4TCNQ. During the vapor doping process, the thin film sample was placed upside down above the glass jar. The sample was kept at a constant temperature of 50 °C during the doping process by using a custom-built sample holder containing a thermoelectric module.

3. Electronic conductivity and Seebeck coefficient measurement

Both electronic conductivity and Seebeck coefficient measurement were performed on samples deposited on top of lithographically-fabricated gold electrodes on quartz substrates. Electronic conductivity was measured either using the 4 point-probe method (for conductivity above 10^{-3} S/cm) or with interdigitated electrodes (IDE) (for conductivity below 10^{-3} S/cm). Four-point probe conductivity gold contacts had a channel length of 0.2 mm and a channel width of 1 mm. Seebeck measurement gold contacts consisted of two 1-mm^2 gold pads adjacent to two 0.2-mm × 1-mm gold bars. The distance between the gold pads (temperature probes and/or voltage probes) and gold bars (voltage probes) was 3 mm apart. Each IDE device has N = 160 gold electrodes, each electrode has the length l of 1 mm, width w of 2 μm and the distance between two adjacent electrode is d = 8 μm. Detailed IDE fabrication process is described in our prior publication.[68]

Four-point probe conductivity measurements were performed using a custom-designed probe station in an argon glove box. Voltage and current measurements were performed using a Keithley 2400 source measure unit and Keithley 6221 precision current source. A constant current was applied to the outer contacts, and the resultant steady-state voltage response was recorded from the inside contacts. The resistance (R; ohms) of the sample was extracted from the slope of the VI sweep using Ohm's law ($V = IR$).

The Seebeck coefficient (α) measurements were performed also in an argon glove box using a custom-built setup. Peltier elements 5 mm apart provided the temperature difference ($\Delta T = T_{hot} - T_{cold}$). A minimal amount of thermal conductive paste was applied to the tips of the thermal couple to ensure good thermal contact between the thermocouple and the gold pads. The voltage probe was either placed on the 1-mm^2 gold pads or 0.2-mm × 1-mm gold bars depending on the magnitude of the conductivity of the sample. A delay of 100 - 200 s was used for voltage measurements to ensure that a steady-state temperature gradient was reached. The Seebeck coefficient was calculated from the slope of a linear fit for the ΔV versus ΔT plot. The measurements were taken within an approximate ΔT of ±3 K around 300 K (room temperature).

Appropriate correction was applied to final Seebeck coefficient calculation depending on the geometry of the voltage and thermal contacts.[69]

4. Grazing incidence wide-angle X-Ray scattering (GIWAXS) and small-angle X-ray scattering (GISAXS)

GIWAXS/GISAXS measurements were performed at beamline 8-ID-E of the Advanced Photon Source, Argonne National Laboratory with 10.86 keV (λ = 0.11416 nm) synchrotron radiation. Samples were enclosed and measured inside a low vacuum chamber (10^{-3} mbar) to minimize concerns about radiation damage as well as to prevent extraneous scattering from ambient air. The measurement time was chosen to be 10 s per frame. For each sample, 3 data sets were taken from 3 adjacent spots on the sample and then summed in order to enhance the signal-to-noise ratio. In our work, the samples were tilted at an angle of incidence of 0.14° with respect to the incoming beam. This angle was chosen to be above the estimated critical angle of sample (*ca.* 0.11°) but below the critical angle of the Si substrates (0.165°). The scattering signal was recorded with a Pilatus 1MF pixel array detector (pixel size = 172 µm) positioned either 228 mm (GIWAXS) or 2185 mm (GISAXS) from the sample. Each data set was stored as a 981×1043 32-bit tiff image with 20-bit dynamic range. The Pilatus detector has rows of inactive pixels at the border between detector modules. In order to fill these gaps, after each measurement the detector was moved to a new vertical direction and the measurement on each spot was repeated, then the gaps were filled by combining the data from two detector positions. Each image was also subjected to detector nonuniformity, detection efficiency, the polarization effect and solid-angle variation correction. Vertical line-cuts were performed as a function of intensity along the q_z direction. All the data processing and extraction were executed using the GIXSGUI package for MATLAB.[70]

5. UV-vis-NIR absorption spectroscopy and Spano model fitting

The UV−vis-NIR absorption spectroscopy measurements were performed using a Shimadzu UV-3600 Plus UV-VIS-NIR Dual Beam Spectrophotometer at the Soft Matter Characterization Facility (SMCF) at the University of Chicago. Absorption spectra of thin films were performed on samples deposited atop quartz substrates whereas solution absorption spectra were obtained by using quartz cells having very short optical pathlength of *ca.* 20 μm.

Quantitative analysis of UV-vis absorption spectra was performed using the Spano model as detailed elsewhere.[47,48] In brief, the cofacial interchain coupling of adjacent conjugated segments in polythiophene leads to a formation of vibration bands, which can be determined using the following Frank-Condon fit to the absorption spectrum:

$$A_{aggregate} \propto \sum_{m=0} \left(\frac{S^m}{m!}\right) \times \left(1 - \frac{We^{-S}}{2E_p} \sum_{n \neq m} \frac{S^n}{n!(n-m)}\right)^2 \times e^{\frac{(\mathrm{E} - \mathrm{E}_0 - \mathrm{mE}_p - \frac{1}{2}\mathrm{WS}^m \mathrm{e}^{-S})^2}{2\sigma^2}}$$

Here, A is the absorption of the aggregates as a function of photon energy, E; S is the Huang-Rhys factor, representing the overlap between vibrational states and assumed to be 1; m corresponds to different energy levels and E_p = 0.179 eV is the energy of C=C symmetric stretch mode. Here, the three fitting parameters are the exciton bandwidth W, the transition energy E_0 and the energetic disorder σ_d (which is the Gaussian width of the absorption peaks)**.**

6. Atomic force microscopy (AFM)

Tapping mode atomic force microscopy (AFM) was performed using the Cypher ES AFM in the University of Chicago MRSEC Facility. AFM micrographs were analyzed and plotted using Gwyddion.[71]

VII. REFERENCE

[1] P. M. Borsenberger, D. S. Weiss, *Organic Photoreceptors for Xerography*, CRC Press,

New York, **1998**.

[2] B. Geffroy, P. le Roy, C. Prat, *Polym. Int.* **2006**, *55*, 572.

[3] K. Müllen, U. Scherf, *Organic Light Emitting Devices: Synthesis, Properties and Applications*, Wiley, New York, **2006**.

[4] H. Sirringhaus, *Adv. Mater.* **2014**, *26*, 1319.

[5] S. Günes, H. Neugebauer, N. S. Sariciftci, *Chem. Rev.* **2007**, *107*, 1324.

[6] R. Kroon, M. Lenes, J. C. Hummelen, P. W. M. Blom, B. de Boer, *Polym. Rev.* **2008**, *48*, 531.

[7] Y. Li, W. K. Tatum, J. W. Onorato, Y. Zhang, C. K. Luscombe, *Macromolecules* **2018**, *51*, 6352.

[8] J. Onorato, V. Pakhnyuk, C. K. Luscombe, *Polym. J.* **2017**, *49*, 41.

[9] A. Loiudice, A. Rizzo, M. Biasiucci, G. Gigli, *J. Phys. Chem. Lett.* **2012**, *3*, 1908.

[10] Y. Zhang, H. Zhou, J. Seifter, L. Ying, A. Mikhailovsky, A. J. Heeger, G. C. Bazan, T.-Q. Nguyen, *Adv. Mater.* **2013**, *25*, 7038.

[11] H. Yan, J. G. Manion, M. Yuan, F. P. García de Arquer, G. R. McKeown, S. Beaupré, M. Leclerc, E. H. Sargent, D. S. Seferos, *Adv. Mater.* **2016**, 6491.

[12] G. Lu, J. Blakesley, S. Himmelberger, P. Pingel, J. Frisch, I. Lieberwirth, I. Salzmann, M. Oehzelt, R. Di Pietro, A. Salleo, N. Koch, D. Neher, *Nat. Commun.* **2013**, *4*, 1588.

[13] B. Lussem, C. M. Keum, D. Kasemann, B. Naab, Z. Bao, K. Leo, *Chem. Rev.* **2016**, *116*, 13714.

[14] S. N. Patel, M. L. Chabinyc, *J. Appl. Polym. Sci.* **2017**, *134*.

[15] R. Kroon, D. A. Mengistie, D. Kiefer, J. Hynynen, J. D. Ryan, L. Yu, C. Müller, *Chem. Soc. Rev.* **2016**, *45*, 6147.

[16] B. Russ, A. Glaudell, J. J. Urban, M. L. Chabinyc, R. A. Segalman, *Nat. Rev. Mater.* **2016**, *1*, 16050.

[17] I. E. Jacobs, A. J. Moulé, *Adv. Mater.* **2017**, *29*, 1.

[18] K. Kang, S. Watanabe, K. Broch, A. Sepe, A. Brown, I. Nasrallah, M. Nikolka, Z. Fei, M. Heeney, D. Matsumoto, K. Marumoto, H. Tanaka, S. Kuroda, H. Sirringhaus, *Nat. Mater.* **2016**, *15*, 896.

[19] J. D. Roehling, J. Li, G. Zhang, M. P. Augustine, *J. Mater. Chem. C* **2016**, *4*, 3454.

[20] D. T. Scholes, S. A. Hawks, P. Y. Yee, H. Wu, J. R. Lindemuth, S. H. Tolbert, B. J. Schwartz, *J. Phys. Chem. Lett.* **2015**, *6*, 4786.

[21] S. N. Patel, A. E. Javier, K. M. Beers, J. A. Pople, V. Ho, R. A. Segalman, N. P. Balsara, *Nano Lett.* **2012**, *12*, 4901.

[22] E. Lim, K. A. Peterson, G. M. Su, M. L. Chabinyc, *Chem. Mater.* **2018**, *30*, 998.

[23] J. Hynynen, D. Kiefer, L. Yu, R. Kroon, R. Munir, A. Amassian, M. Kemerink, C. Müller, *Macromolecules* **2017**, *50*, 8140.

[24] B. X. Dong, Z. Liu, M. Misra, J. Strzalka, J. Niklas, O. Poluektov, F. A. Escobedo, C. K. Ober, P. F. Nealey, S. N. Patel, *ACS Nano* **2019**, *13*, 7665−7675.

[25] J. Gao, B. W. Stein, A. K. Thomas, J. A. Garcia, J. Yang, M. L. Kirk, J. K. Grey, *J. Phys. Chem. C* **2015**, *119*, 16396.

[26] I. Salzmann, G. Heimel, M. Oehzelt, S. Winkler, N. Koch, *Acc. Chem. Res.* **2016**, *49*, 370.

[27] S. N. Patel, A. M. Glaudell, K. A. Peterson, E. M. Thomas, K. A. O'Hara, E. Lim, M. L. Chabinyc, *Sci. Adv.* **2017**, *3*, e1700434.

[28] V. Untilova, T. Biskup, L. Biniek, V. Vijayakumar, M. Brinkmann, *Macromolecules* **2020**, *53*, 2441.

[29] V. Vijayakumar, P. Durand, H. Zeng, V. Untilova, L. Herrmann, P. Algayer, N. Leclerc, M. Brinkmann, *J. Mater. Chem. C* **2020**, *8*, 16470.

[30] D. A. Stanfield, Y. Wu, S. H. Tolbert, B. J. Schwartz, *Chem. Mater.* **2021**, *33*, 2343.

[31] V. Vijayakumar, Y. Zhong, V. Untilova, M. Bahri, L. Herrmann, L. Biniek, N. Leclerc, M. Brinkmann, *Adv. Energy Mater.* **2019**, *1900266*, 1.

[32] Y. Wang, L. Yang, X. Shi, X. Shi, L. Chen, M. S. Dargusch, J. Zou, Z. Chen, *Adv. Mater.* **2019**, *1807916*, 1807916.

[33] M. Goel, M. Thelakkat, *Macromolecules* **2020**.

[34] G. Zuo, H. Abdalla, M. Kemerink, *Adv. Electron. Mater.* **2019**, *1800821*, 1.

[35] Y. Xue, C. Gao, L. Liang, X. Wang, G. Chen, *J. Mater. Chem. A* **2018**, *6*, 22381.

[36] B. T. McGrail, A. Sehirlioglu, E. Pentzer, *Angew. Chemie - Int. Ed.* **2015**, *54*, 1710.

[37] D. Kiefer, L. Yu, E. Fransson, A. Gómez, D. Primetzhofer, A. Amassian, M. Campoy-Quiles, C. Müller, *Adv. Sci.* **2017**, *4*.

[38] J. Liu, L. Qiu, R. Alessandri, X. Qiu, G. Portale, J. J. Dong, W. Talsma, G. Ye, A. A. Sengrian, P. C. T. Souza, M. A. Loi, R. C. Chiechi, S. J. Marrink, J. C. Hummelen, L. J. A. Koster, *Adv. Mater.* **2018**, *30*, 1.

[39] G. Lu, L. Bu, S. Li, X. Yang, *Adv. Mater.* **2014**, *26*, 2359.

[40] H. A. Bronstein, C. K. Luscombe, *J. Am. Chem. Soc.* **2009**, *131*, 12894.

[41] J. P. Coote, J. S. Kim, B. Lee, J. Han, B. J. Kim, G. E. Stein, *Macromolecules* **2018**, *51*, 9276.

[42] J. S. Kim, Y. Kim, H. J. Kim, H. J. Kim, H. Yang, Y. S. Jung, G. E. Stein, B. J. Kim, *Macromolecules* **2017**, *50*, 1902.

[43] V. Ho, B. W. Boudouris, B. L. McCulloch, C. G. Shuttle, M. Burkhardt, M. L. Chabinyc,

R. A. Segalman, *J. Am. Chem. Soc.* **2011**, *133*, 9270.

[44] H. Luo, C. Yu, Z. Liu, G. Zhang, H. Geng, Y. Yi, K. Broch, Y. Hu, A. Sadhanala, L. Jiang, P. Qi, Z. Cai, H. Sirringhaus, D. Zhang, *Sci. Adv.* **2016**, *2*, 1.

[45] B. X. Dong, C. Nowak, J. W. Onorato, J. Strzalka, F. A. Escobedo, C. K. Luscombe, P. F. Nealey, S. N. Patel, *Chem. Mater.* **2019**, *31*, 1418.

[46] W. Liu, L. Müller, S. Ma, S. Barlow, S. R. Marder, W. Kowalsky, A. Köhn, R. Lovrincic, *J. Phys. Chem. C* **2018**, 27983−27990.

[47] F. C. Spano, *J. Chem. Phys.* **2005**, *122*, 234701.

[48] F. C. Spano, *Chem. Phys.* **2006**, *325*, 22.

[49] J. Clark, J.-F. Chang, F. C. Spano, R. H. Friend, C. Silva, *Appl. Phys. Lett.* **2009**, *94*, 163306.

[50] B. G. Kim, M. S. Kim, J. Kim, *ACS Nano* **2010**, *4*, 2160.

[51] J. Hynynen, D. Kiefer, C. Müller, *RSC Adv.* **2018**, *8*, 1593.

[52] S. N. Patel, A. E. Javier, G. M. Stone, S. A. Mullin, N. P. Balsara, *ACS Nano* **2012**, *6*, 1589.

[53] X. Liu, K. S. Jeong, B. P. Williams, K. Vakhshouri, C. Guo, K. Han, E. D. Gomez, Q. Wang, J. B. Asbury, *J. Phys. Chem. B* **2013**, *117*, 15866.

[54] H. J. Snaith, M. Grätzel, *Appl. Phys. Lett.* **2006**, *89*.

[55] B. A. Gregg, S. G. Chen, H. M. Branz, *Appl. Phys. Lett.* **2004**, *84*, 1707.

[56] D. Mombrú, M. Romero, R. Faccio, Á. W. Mombrú, *J. Phys. Chem. C* **2020**, *124*, 7061.

[57] S. N. Patel, Synthesis and Characterization of Simultaneous Electronic and Ionic Conducting Block Copolymers for Lithium Battery Electrodes, UC Berkeley, **2013**.

[58] D. T. Scholes, P. Y. Yee, J. R. Lindemuth, H. Kang, J. Onorato, R. Ghosh, C. K.

Luscombe, F. C. Spano, S. H. Tolbert, B. J. Schwartz, *Adv. Funct. Mater.* **2017**, *27*, 1.

[59] W. Shi, E. Yildirim, G. Wu, Z. M. Wong, T. Deng, J. S. Wang, J. Xu, S. W. Yang, *Adv. Theory Simulations* **2020**.

[60] J. Liu, Y. Shi, J. Dong, M. I. Nugraha, X. Qiu, M. Su, R. C. Chiechi, D. Baran, G. Portale, X. Guo, L. J. A. Koster, *ACS Energy Lett.* **2019**, *4*, 1556.

[61] W. Shi, T. Zhao, J. Xi, D. Wang, Z. Shuai, *J. Am. Chem. Soc.* **2015**, *137*, 12929.

[62] Y. Xuan, X. Liu, S. Desbief, P. Leclère, M. Fahlman, R. Lazzaroni, M. Berggren, J. Cornil, D. Emin, X. Crispin, *Phys. Rev. B - Condens. Matter Mater. Phys.* **2010**, *82*, 1.

[63] H. Fritzsche, *Solid State Commun.* **1971**, *9*, 1813.

[64] S. Dongmin Kang, G. Jeffrey Snyder, *Nat. Mater.* **2017**, *16*, 252.

[65] K. Kang, S. Schott, D. Venkateshvaran, K. Broch, G. Schweicher, D. Harkin, C. Jellett, C. B. Nielsen, I. McCulloch, H. Sirringhaus, *Mater. Today Phys.* **2019**, *8*, 112.

[66] A. Abutaha, P. Kumar, E. Yildirim, W. Shi, S. W. Yang, G. Wu, K. Hippalgaonkar, *Nat. Commun.* **2020**, *11*, 1.

[67] S. A. Gregory, R. Hanus, A. Atassi, J. M. Rinehart, J. P. Wooding, A. K. Menon, M. D. Losego, G. J. Snyder, S. K. Yee, *Nat. Mater.* **2021**.

[68] D. Sharon, P. Bennington, C. Liu, Y. Kambe, B. X. Dong, V. F. Burnett, M. Dolejsi, G. Grocke, S. N. Patel, P. F. Nealey, *J. Electrochem. Soc.* **2018**, *165*, H1028.

[69] S. Van Reenen, M. Kemerink, *Org. Electron. physics, Mater. Appl.* **2014**, *15*, 2250.

[70] Z. Jiang, *J. Appl. Crystallogr.* **2015**, *48*, 917.

[71] D. Nečas, P. Klapetek, *Cent. Eur. J. Phys.* **2012**, *10*, 181.

The thermoelectric properties of a conjugated block copolymer P3HT-b-POEM are investigated. The introduction of POEM block enables solution co-processing with an ionic salt, resulting in significant improvement in molecular order of P3HT block. Subsequent doping with F4TCNQ results in a thermoelectric power factor of 13.0 $\mu Wm^{-1}K^{-2}$, which is more than 20 times higher than salt-free P3HT-*b*-POEM sample.

Ban Xuan Dong[1], Ziwei Liu[2], Jonathan W. Onorato[3], Tengzhou Ma[1], Joseph Strzalka[4], Peter Bennington[1], Christine K. Luscombe[3,5,6], Christopher K. Ober[2], Paul F. Nealey[1,7], Shrayesh N. Patel[1,*]

Ionic Dopant-Induced Ordering Enhances the Thermoelectric Properties of a Polythiophene-Based Block Copolymer

Table of content